

A Novel Attention Mechanism Using Anatomical Prior Probability Maps for Thoracic Disease Classification from X-Ray Images

Md. Iqbal Hossain[†], S. M. Jawaad Hossain[†], Mohammad Zunaed and Taufiq Hasan, *Senior Member, IEEE*

Abstract— Computer-aided disease diagnosis and prognosis based on medical images is a rapidly emerging field. Many Convolutional Neural Network (CNN) architectures have been developed by researchers for disease classification and localization from chest X-ray images. It is known that different thoracic disease lesions are more likely to occur in specific anatomical regions compared to others. Based on this knowledge, we first estimate a disease-dependent spatial probability, i.e., an *anatomical prior*, that indicates the probability of occurrence of a disease in a specific region in a chest X-ray image. Next, we develop a novel attention-based classification model that combines information from the estimated *anatomical prior* and automatically extracted chest region of interest (ROI) masks to provide attention to the feature maps generated from a deep convolution network. Unlike previous works that utilize various self-attention mechanisms, the proposed method leverages the extracted chest ROI masks along with the probabilistic *anatomical prior* information, which selects the region of interest for different diseases to provide attention. The proposed method shows superior performance in disease classification on the NIH ChestX-ray14 dataset compared to existing state-of-the-art methods while reaching an area under the ROC curve (AUC) of 0.8427. Regarding disease localization, the proposed method shows competitive performance compared to state-of-the-art methods, achieving an accuracy of 61% with an Intersection over Union (IoU) threshold of 0.3. The proposed method can also be generalized to other medical image-based disease classification and localization tasks where the probability of occurrence of the lesion is dependent on specific anatomical sites.

Index Terms— Thoracic disease classification, anatomical prior, chest X-Ray, anatomy-aware attention.

I. INTRODUCTION

Thoracic disorders are one of the major health concerns worldwide as the heart and lungs, two vital human organs, are located within the thorax. In 2017, around 544.9 million people were affected by chronic respiratory illness [1], a thoracic disease, leading to 3.9 million deaths [2]. Different medical

[†]Md. Iqbal Hossain and S. M. Jawaad Hossain contributed equally and share the first authorship.

Md. Iqbal Hossain, S. M. Jawaad Hossain, Mohammad Zunaed, and Taufiq Hasan are with the mHealth Lab, Department of Biomedical Engineering, Bangladesh University of Engineering and Technology, Dhaka-1205, Bangladesh (e-mails: mdiqbalhosain@gmail.com, jawaad.1695@gmail.com, rafizunaed@gmail.com, taufiq@bme.buet.ac.bd).

imaging modalities, e.g., X-ray, Magnetic Resonance Imaging (MRI), and Computed Tomography (CT) can diagnose different thoracic disorders. The chest X-ray (CXR) remains the most commonly performed and widely available radiological diagnostic method to assess and diagnose these diseases. The chest radiograph is an X-ray projection image of the thoracic cavity used to diagnose conditions affecting the chest, its contents, and nearby structures. It is one of the most effective and low-cost methods for diagnosing thoracic diseases. Since CXR is a projection imaging method providing a 2D image of the 3D human body, anatomical structures are overlapped in the resulting image. Therefore, diagnosis of diseases with CXR image highly depends on the skill and experience of the radiologist [3]. However, in many underserved regions of the world, the number of skilled radiologists is insufficient. In such scenarios, automated CXR image interpretation using artificial intelligence (AI) can significantly benefit health systems. This is true even if the algorithms are not making full autonomous decisions and are only used to assist physicians.

Different thoracic disease lesions have unique characteristics and are identified in specific regions of a chest radiography image. For example, when identifying pneumonia, a radiologist will look for white spots in the lungs that show the characteristics of infection. In contrast, the opacity features of pleural effusion manifest in the pleural space, not inside the lung fields. Thus we may consider that the diagnostic features of different thoracic diseases have a higher probability of occurrence in certain anatomical regions of the chest X-ray. Consequently, specific disease features may have a zero probability of occurrence in certain anatomical regions (e.g., observing consolidation features outside the lungs). Therefore, to reliably detect and localize thoracic diseases, we not only require deep learning-based models to learn the disease-specific features but also to focus on the specific anatomical regions where the likelihood of the disease is highest.

In the research literature, different attention-based methods [4]–[6] have been used for medical disease diagnosis where the model automatically learns to identify and focus on the regions of interest containing the lesions. However, these methods are data-driven and are generally agnostic to the human anatomy and its dependence on identifying the diseased regions. Chen et al. [7] and Kamal et al. [8] utilized lung segmentation-based attention mechanisms. However, disease-specific anatomical prior knowledge was not considered within

the attention mechanism and abnormality localization.

Considering the limitations of previous works in this area, we propose using two attention mechanisms: chest ROI mask-based attention and disease-specific anomaly-based attention method utilizing an anatomical prior probabilistic map of lesion location. The main contributions of this paper are as follows:

- We utilize existing bounding box annotation on disease localization to identify the region of interest for finding a particular disease within an X-ray image.
- We propose an anatomy prior attention module, which can be used on both chest ROI and abnormality-based masks to provide spatial attention to the region of interest.
- We employ only a single model for both the classification and localization task, where the latter is performed using an unsupervised approach.

II. RELATED WORKS

A. Attention Mechanism

Attention modules available in the computer vision literature can be divided into two main categories. One includes the Squeeze-and-Excitation (SE) approach that adaptively recalibrates channel-wise feature responses by explicitly modeling inter-dependencies between channels [9]. The other is Gather-Excite (GE) method which efficiently aggregates feature responses from a large spatial extent and excites, redistributing the pooled information to local features [10]. Chen et al. [11] presented a non-local (NL) attention module to utilize the local relationship for capturing long-range dependencies. However, none of these modules use a segmentation mask or probability distribution of the spatial occurrence of diseases to provide attention within a CNN.

Zhou et al. [12] used class activation mapping (CAM) to identify discriminative regions by a linearly weighted combination of activation maps of the last convolutional layer before the global pooling layer. The prerequisite of applying CAM requires a single convolutional layer after a global pooling layer, which makes the final prediction. However, all models are not designed to have a global pooling layer and don't have a single convolutional layer after the global pooling layer. On the hand Grad-CAM [13], Grad-CAM++ [14], Score-CAM [15], SS-CAM [16], XGrad-CAM [17] are not restricted by these types of requirements and produce excellent result compared to CAM. Ye et al. [18] have used a modified version of CAM for the attention mechanism. Xu et al. [19] has used Grad-CAM for channel-spatial attention. However, the drawback of these types of gradient-based activation map generation is that they can not be used directly in the training phases due to high computational costs, and they are only used during the inference phase.

B. Multi-label CXR Image Classification

Computer-aided chest X-ray disease screening was first introduced by Lodwick et al. [20]. With the recent advancements in artificial intelligence and enhanced computational capabilities, many deep learning algorithms have been presented to

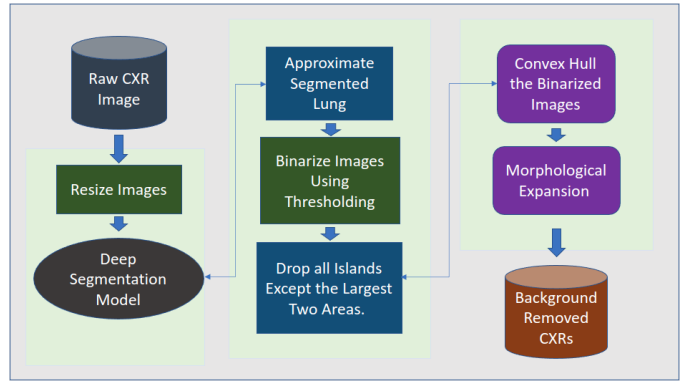


Fig. 1. A flow-diagram of the chest ROI mask generation module.

identify diseases in CXR images. Wang et al. [21] released a large multi-class CXR dataset, namely, the NIH ChestX-ray14 for chest disease diagnosis using machine learning. The public release of this dataset has motivated many subsequent research publications [18], [22], [23].

In the case of disease localization on CXR images, many works have also been published previously [21], [24], [25] where the region of interest labels was not directly used. The NIH ChestX-ray14 has since become a benchmark dataset for evaluating weakly-supervised disease localization algorithms as it also includes bounding box annotations identifying the diseased regions. Among notable previous work on localization, Ye et al. [18] used probabilistic-CAM Pooling to generate probable disease locations and Ouyang et al. [26] used hierarchical attention for weakly supervised abnormality localization. Although these methods have used some form of attention mechanism within the architecture, the methods still depend on a data-driven approach to identifying the diseased regions. Since the CXR image represents a human anatomical structure that has some predictable properties, it is thus expected that disease-specific anatomical prior information can be beneficial in designing attention-based deep learning models for the classification and localization of diseases.

III. PROPOSED METHOD

This section describes our proposed approach, where we use a deep learning-based novel attention module, named Anatomical Prior Attention Module (APAM), that utilizes both the chest ROI mask and a disease-specific anatomical prior distribution map for pathology classification and localization. We also describe in detail the extraction of the chest ROI mask and the generation of a disease-specific anatomical prior probability map.

A. Chest ROI Mask Generation

We employ the well-established U-net [27] segmentation model to extract the lung regions from the input CXR images. We train the model using the 247 images from the JSRT dataset [28]. The segmentation model produces undesirable small islands in the case of some images. To address these issues, we binarize and apply post-processing to the segmentation results to remove the unwanted islands based on

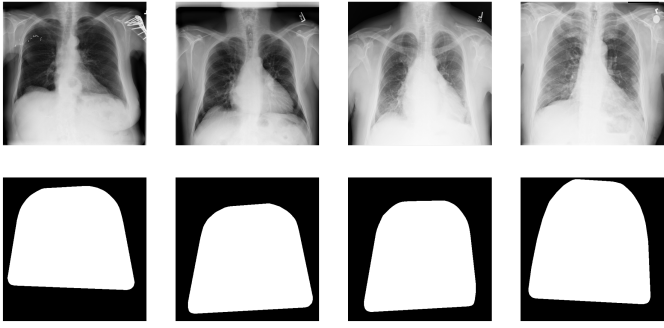


Fig. 2. Examples of some generated chest ROI masks. Top panel: Example input CXR images, Bottom panel: Corresponding chest ROI masks of the example CXR images.

the anatomical characteristics of the lungs. Since all other islands are small compared to the lung islands, we filter out the largest two islands representing the right and left lung. The sternum region is also important for some thoracic diseases and contains crucial information for classification. To retain this region, we use the convex hull operation [29]. Finally, we use morphological expansion to retain further information from the pleural regions. The overall chest ROI mask generation flow chart is provided in Fig. 1. Some of the CXR images and their corresponding generated masks are shown in Fig. 2.

B. Generating Disease-specific Anatomical Prior Probability Map

We compute the disease-specific anatomical prior probability maps by identifying the spatial regions of the CXR images where the lesions are most likely to occur. To construct this map, we use the NIH Chest X-ray dataset, which includes 880 bounding-box annotated images identifying the regions of the abnormality [21]. First, we create a binary image keeping the bounding-box interior spatial values equal to 1 and the rest equal to 0 for a particular disease. We then take the sum of all binary images of a particular disease to generate unnormalized probability map. Finally, we normalize pixel values of the unnormalized probability map by dividing them by the maximum pixel value within that probability map. The normalized mask is used in the network as the anatomical prior probability map for providing disease-specific attention.

Let $I_c^k(i, j)$ indicate the pixel position (i, j) of the k^{th} constructed binary mask image from the bounding box annotated ground truth image for the disease class c . The disease-specific anatomical prior probability map M_c^p is generated as follows. First, we obtain the unnormalized raw probability map as,

$$\hat{M}_c(i, j) = \sum_{k=1}^{N_c} I_c^k(i, j) \quad (1)$$

where N_c indicates the number of CXR images available for the disease class c . Next, we normalize the raw map \hat{M}_c to obtain the final anatomical prior probability map by,

$$M_c^p(i, j) = \frac{\hat{M}_c(i, j)}{\max(\hat{M}_c)} \quad (2)$$

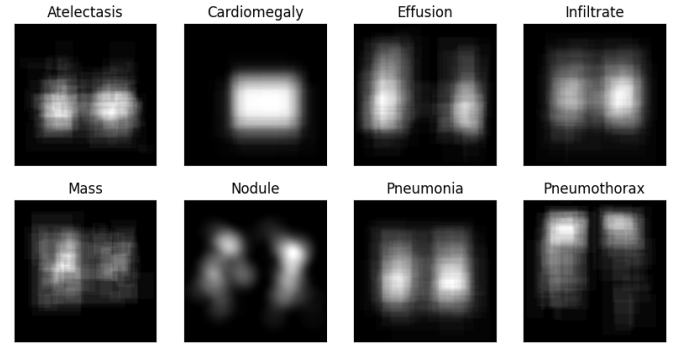


Fig. 3. Disease-specific anatomical prior probability maps generated for the 8 diseases for which the bounding box annotations are available in the NIH dataset.

Here, the max operation identifies the maximum pixel value of the raw probability map \hat{M}_c . Finally, these anatomical prior probability maps were generated for all eight diseases for which the bounding box annotations are available. Figure 3 shows the generated disease-specific anatomical prior probability maps for the eight abnormalities. In the strictest sense, the obtained maps $M_c(i, j)$ do not represent an actual probability distribution. Firstly, this is because the regions are obtained from the bounding box information that is larger than the actual disease regions. Secondly, obtaining a probability distribution requires that the integration over the entire map should equal unity. However, we only normalize the map using the highest pixel value so that it does not contain very small numerical values. In actual implementation, the map's relative intensity values are more important than the absolute values. For, disease classes whose bounding-box annotations are not available, we use $M_c^p(i, j) = 1$.

C. Anatomical Prior Attention Module (APAM)

In this section, we describe the proposed anatomical prior attention module (APAM), which takes a feature map and a mask (chest ROI mask or anomaly probability map) as inputs to generate an attention map by providing spatial attention to the feature map. First, we multiply the feature map with the input mask to generate a masked feature map. Later, we take the weighted sum of the feature map and masked feature map to retain information from the region outside the mask since some disease predictions may depend on the feature of the unmasked region. The weights are generated from the feature map and the masked feature map through a CNN. To learn the weights, we use a network similar to the channel-wise attention module described in [30]. However, unlike [30], we aggregate spatial information from both the feature map and the masked feature map.

Let $\mathbf{F} \in \mathbb{R}^{C \times H \times W}$ be the feature map generated by the backbone CNN network and $\mathbf{M}_{inp} \in \mathbb{R}^{1 \times H \times W}$ be the input mask (chest ROI mask or anomaly probability map) resized to the spatial dimension of feature map \mathbf{F} . We pass the feature map \mathbf{F} into two pooling layers: global average pooling (AvgPool) and global max pooling (MaxPool). The two corresponding outputs from these pooling layers are denoted as \mathbf{F}_{avg} and \mathbf{F}_{max} , respectively, where $\mathbf{F}_{avg}, \mathbf{F}_{max} \in \mathbb{R}^{C \times 1 \times 1}$.

Again, let $\mathbf{F}_m \in \mathbb{R}^{C \times H \times W}$ be the masked feature map which is produced after we multiply the feature map \mathbf{F} with the input mask \mathbf{M}_{inp} . We obtain $\mathbf{M}_{avg}, \mathbf{M}_{max} \in \mathbb{R}^{C \times 1 \times 1}$ after passing \mathbf{M} through the global average pooling and global max pooling layers in a similar way.

$$\mathbf{F}_m = \mathbf{F} \odot \mathbf{M}_{inp} \quad (3)$$

$$\mathbf{F}_{avg} = \text{AvgPool}(\mathbf{F}) \quad (4)$$

$$\mathbf{F}_{max} = \text{MaxPool}(\mathbf{F}) \quad (5)$$

$$\mathbf{M}_{avg} = \text{AvgPool}(\mathbf{M}) \quad (6)$$

$$\mathbf{M}_{max} = \text{MaxPool}(\mathbf{M}) \quad (7)$$

Here, \odot denotes element wise multiplication. Furthermore, instead of shared multi-layered perceptron (MLP), we use separate MLPs for all four spatial context descriptors ($\mathbf{F}_{avg}, \mathbf{F}_{max}, \mathbf{M}_{avg}, \mathbf{M}_{max}$). After passing the spatial context descriptors through the CNN, the network produces the required weight vector $\mathbf{W} \in \mathbb{R}^{C \times 1 \times 1}$. The mathematical equation for generating the weight vector \mathbf{W} is provided below:

$$\begin{aligned} \mathbf{W} = \text{CB}_5 & \left[\text{CB}_1(\mathbf{F}_{avg}) + \text{CB}_2(\mathbf{F}_{max}) + \right. \\ & \left. \text{CB}_3(\mathbf{M}_{avg}) + \text{CB}_4(\mathbf{M}_{max}) \right] \end{aligned} \quad (8)$$

Here, $\text{CB}_1, \text{CB}_2, \dots, \text{CB}_5$ indicates the convolutional blocks. Each block consists of one convolutional layer followed by a batch normalization layer and a non-linear activation function. In CB_5 , we use the sigmoid activation function so that the components of weight \mathbf{W} are within the range $[0, 1]$. For the other four convolutional blocks, we use the leaky ReLU with a negative slope of 0.2 to mitigate the vanishing gradient problem [31]. Finally, we generate the attention map $\mathbf{A} \in \mathbb{R}^{C \times H \times W}$ from the weighted sum of \mathbf{F} and \mathbf{F}_m using the formula below:

$$\mathbf{A} = \mathbf{W} \odot \mathbf{F} + (1 - \mathbf{W}) \odot \mathbf{F}_m \quad (9)$$

A schematic diagram of APAM is shown in Fig. 4.

D. Classification and Localization

At first, we extract a feature map from the input image with a CNN backbone. We have used DenseNet-121 [32] as backbone for feature extraction. Then we use our proposed APAM to generate an attention map from the extracted feature map. For generating attention maps from the feature map, we have used the image-specific chest ROI mask described previously with APAM to generate ROI attention map \mathbf{A}_{ROI} .

$$\mathbf{A}_{ROI} = \mathbf{W}_{ROI} \odot \mathbf{F} + (1 - \mathbf{W}_{ROI}) \odot \mathbf{F}_{ROI} \quad (10)$$

Here, \mathbf{W}_{ROI} is the weight generated by APAM from feature map \mathbf{F} and masked feature map \mathbf{W}_{ROI} . Then, we have used K ($K = \text{number of abnormalities}$) numbers of disease-specific anatomy prior probability maps with APAM to generate K disease-specific attention maps \mathbf{A}_p^c .

$$\mathbf{A}_p^c = \mathbf{W}_p^c \odot \mathbf{F} + (1 - \mathbf{W}_p^c) \odot \mathbf{F}_p^c, \quad c \in \{1, \dots, K\} \quad (11)$$

Here, \mathbf{W}_p^c is the weight generated by APAM from feature map \mathbf{F} and masked feature map \mathbf{F}_p^c of abnormality c . Then

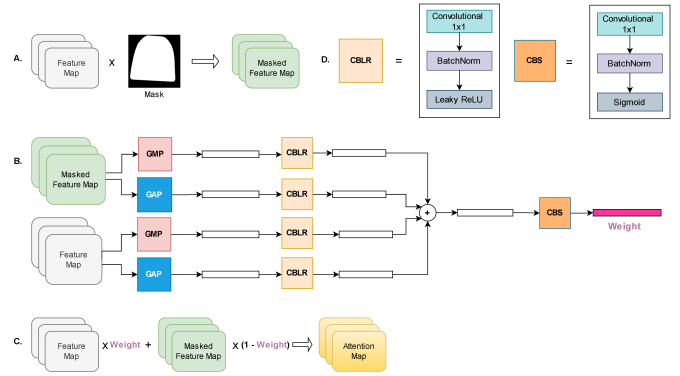


Fig. 4. A schematic diagram of the proposed Anatomy Prior Attention Module (APAM); A: Mask is multiplied with the feature map to generate a masked feature map; B: Weight is dynamically calculated from the feature map through a CNN model. Here, GMP = Global Max Pooling and GAP = Global Average Pooling; C: Weighted sum of the feature map and masked feature map is calculated with the aforementioned weight to produce the final attention map; D: A schematic elaborating different parts of the CNN responsible for calculating the final weight.

for predicting the probability of each disease, the image-specific ROI attention map and the disease-specific attention map of that particular disease are channel-wise concatenated to produce a disease-specific concatenated map.

$$\mathbf{A}_{cat}^c = \text{concat}(\mathbf{A}_{ROI}, \mathbf{A}_p^c), \quad c \in \{1, \dots, K\} \quad (12)$$

Here, $\mathbf{A}_{cat}^c \in \mathbb{R}^{2C \times H \times W}$. These concatenated maps are passed through individual global pooling and then 1×1 convolutional layers sequentially to generate the probability of that disease. And we have used the same convolutional layers on the concatenated feature maps to generate individual heatmap using CAM method. The schematic of this model is shown in Fig. 5.

We have also tried predicting disease probabilities and localization results only from disease-specific probability maps which produced better localization results than the previous method but inferior results in terms of classification.

As we have used 224×224 images as input, the produced feature map is only 7×7 in size. This size is minimal for localizing diseases with small features like mass or nodule. Therefore, we have tried to incorporate the feature pyramid network (FPN) [33] to enhance the spatial resolution of our feature map to 14×14 before passing through APAM. In addition to traditional FPN which utilizes addition for combining features from different layers of backbone, we have also used a variation of FPN which uses channel-wise feature concatenation instead of addition as used in Yolo-V3 [34].

IV. IMPLEMENTATIONAL DETAILS

A. Data Resources

We evaluate the proposed APAM-based architecture on the NIH ChestX-Ray14 and CheXpert datasets. These data resources are briefly described below.

NIH ChestX-Ray14: The NIH ChestX-Ray14 contains 112,120 frontal chest X-ray images from 32,717 unique patients [21]. All these images are annotated for 15 classes (14 diseases along with “No Findings”). Within this dataset,

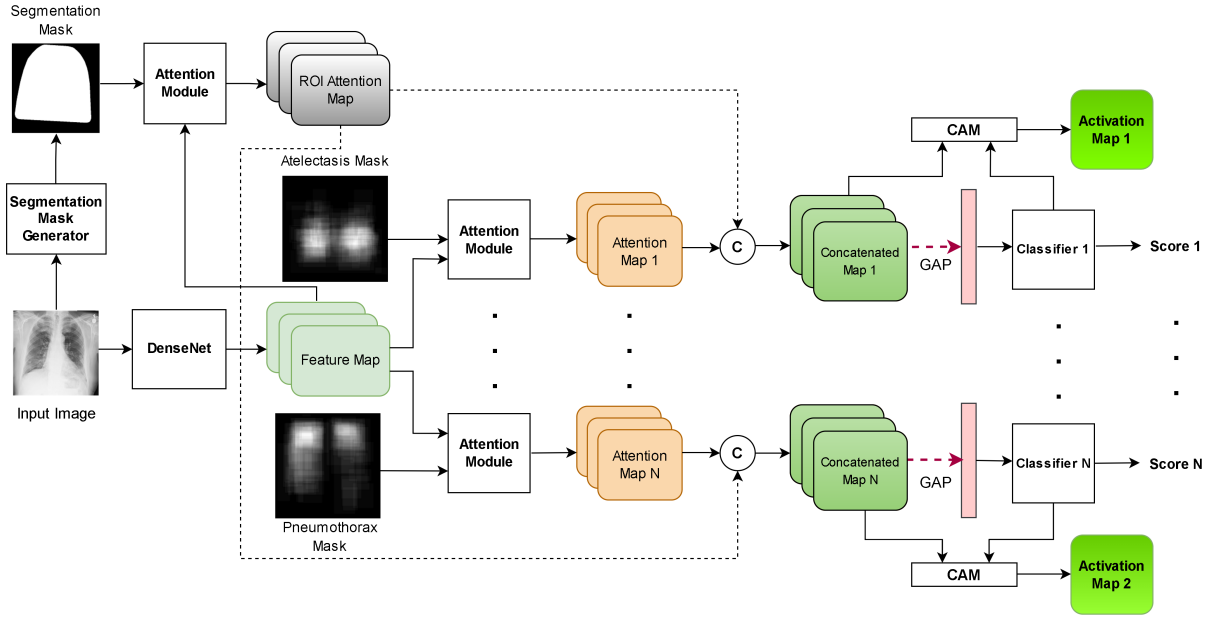


Fig. 5. A schematic of the proposed model for disease classification from CXR utilizing both lung segmentation attention and disease-specific attention.

880 images are specially annotated by a bounding box for the localization of 8 diseases. In our classification experiments, we use 70%, 10%, and 20% data for training, cross-validation, and testing, respectively. We train and test our model on the classification data for all 15 classes. On the other hand, we use the bounding-box annotated data of the 8 classes to assess the disease localization performance of our model.

CheXpert: The CheXpert dataset [35] is a chest X-ray dataset containing class label annotation of 14 classes (13 diseases along with “No Findings”). Other than positive and negative labels for each class, the dataset also contains an uncertainty label for some images. The dataset consists of 224,316 chest X-ray images for training and 230 chest X-ray images for validation. We use only frontal view chest X-ray images from this dataset. If we consider only images with a frontal view, there are about 200,000 chest X-ray images for training and 200 images for validation in the dataset. We use this dataset for the classification of five thoracic diseases, namely, atelectasis, cardiomegaly, consolidation, edema, and pleural effusion.

B. Data Preparation

We first normalize the pixel values of chest X-ray images with the mean and standard deviation of pixels from the ImageNet dataset [36]. Next, we resize the image to 256×256 pixels. Afterward, the training images are randomly cropped to 224×224 pixels. The validation and test images are center-cropped to 224×224 pixels. We use the same resizing and cropping method for the corresponding anatomy prior maps and chest ROI masks. In the case of CheXpert dataset preparation (image augmentation, dealing with class imbalance, uncertain labels, etc.), we use the same procedure described in [18]. We use the same disease-specific anatomy prior maps computed from the NIH dataset for the CheXpert dataset.

C. Training Parameters

We use a batch size of 16 and train all of our models for 15 epochs. We use binary cross entropy as the loss function, and the Adam optimizer [37] with an initial learning rate of 0.0001 and weight decay of 0.0001. We use an exponential learning rate scheduler during training, which decreases the learning rate after every 4 epochs by multiplying it by 0.1.

D. Activation Map and Bounding Box Generation

We use class activation maps (CAM) for heatmap generation. For the generation of bounding boxes from the heatmap map, to evaluate localization performance, we first convert the activation map or heatmap to a binary mask using binary thresholding with a threshold value of 127. Next, we use the algorithm introduced by [38] to find the contours of the regions inside the binary mask and prepare bounding boxes around the contours by taking extreme boundary values of the contours as the edge of our bounding boxes.

E. Evaluation Metrics

We use ROC-AUC (Receiver Operating Characteristic-Area Under Curve), also abbreviated as AUC, to measure the classification performance of our model on the NIH test data. Furthermore, we use the ratio of the number of cases with correct localization against the total number of cases in each class to report the localization performance of our models on 880 bounding-box annotated data of the NIH dataset. Here, we use IoU (Intersection over Union) between the predicted bounding box and ground-truth to detect correct localization following prior work [21], [26], [39]. In this case, the localization result is regarded as correct if $IoU > T(IoU)$ where $T(IoU)$ is the threshold for localization.

TABLE I
ABLATION STUDY: AUC SCORES OF OUR TRAINED MODELS ON NIH DATASET. THE BEST RESULTS ARE SHOWN IN BOLD FONT.

Model				AUC Score (%)														
FPN_T	FPN_C	AM (AbM)	AM (LM)	Atel	Card	Effu	Infi	Mass	Nodu	Pne1	Pne2	Cons	Edem	Emph	Fibr	PT	Hern	Mean
Baseline				81.79	90.82	88.37	70.82	85.15	79.23	78.01	87.72	80.55	89.79	91.77	85.08	77.96	90.67	84.12
✓				82.47	91.51	88.42	70.78	85.35	78.88	76.46	87.84	80.92	89.46	91.63	84.59	78.66	84.28	83.66
	✓			82.05	90.58	88.36	70.67	84.92	78.81	77.15	87.13	80.20	88.78	91.70	83.22	78.28	86.28	83.44
		✓		82.74	90.95	88.37	70.73	85.19	79.15	76.72	88.02	80.93	89.51	91.93	84.37	78.90	91.36	84.20
			✓	82.40	90.70	88.54	71.05	85.00	78.73	76.99	87.14	80.84	89.22	91.81	83.83	78.70	88.46	83.81
✓		✓		82.40	91.19	88.51	70.63	85.22	79.13	76.38	87.03	80.67	88.72	91.38	82.95	78.54	86.88	83.54
	✓	✓		82.46	91.37	88.61	70.71	85.64	78.76	76.45	87.56	80.75	89.27	92.01	83.68	78.56	86.95	83.77
		✓	✓	82.38	91.36	88.46	70.99	85.12	79.16	78.54	87.35	80.86	89.72	92.04	83.55	78.42	91.83	84.27
✓			✓	82.36	91.30	88.36	70.36	85.57	79.22	77.62	87.91	80.66	88.61	91.96	82.54	77.54	84.81	83.49
	✓		✓	81.97	90.40	88.11	70.55	84.85	78.91	76.30	87.13	80.38	88.64	91.46	83.37	77.68	86.52	83.31
✓		✓	✓	82.49	91.45	88.32	70.79	85.63	78.90	77.69	88.07	80.58	88.66	91.57	82.66	78.40	86.54	83.70
	✓	✓	✓	82.49	91.34	88.42	70.69	85.16	78.51	77.43	87.11	80.59	88.92	91.97	83.32	77.87	83.61	83.39

Here, FPN_T = Traditional FPN, FPN_C = FPN Using Concatenation, AM (AbM) = APAM Utilizing Probabilistic Abnormality Mask, AM(LM) = APAM Utilizing Chest ROI Mask, Atel = Atelectasis, Card = Cardiomegaly, Effu = Effusion, Infi = Infiltration, Nodu = Nodule, Pne1 = Pneumonia, Pne2 = Pneumothorax, Cons = Consolidation, Edem = Edema, Emph = Emphysema, Fibr = Fibrosis, PT = Pleural Thickening, Hern = Hernia

TABLE II

COMPARISON OF CLASSIFICATION ACCURACY (%) OF OUR BEST PERFORMING MODEL WITH STATE-OF-THE-ART METHODS ON THE NIH DATASET. THE BEST RESULTS ARE SHOWN IN BOLD FONT.

Model	Atel	Card	Effu	Infi	Mass	Nodu	Pne1	Pne2	Cons	Edem	Emph	Fibr	PT	Hern	Mean
DCNN [21]	71.60	80.70	78.40	60.90	70.60	67.10	63.30	80.60	70.80	83.50	81.50	76.90	70.80	76.70	73.81
LSTM-Net [40]	73.30	85.80	80.60	67.50	72.70	77.80	69.00	80.50	71.70	80.60	84.20	75.70	72.40	82.40	76.73
TieNet [41]	73.20	84.40	79.30	66.60	72.50	68.50	72.00	84.70	70.10	82.90	86.50	79.60	73.50	87.60	77.24
AGCL [24]	75.57	88.65	81.91	68.92	81.36	75.45	72.92	84.99	72.83	84.75	90.75	81.79	76.47	87.47	80.27
Ho et al. [42]	79.50	88.70	87.50	70.30	83.50	71.60	74.20	86.30	78.60	89.20	87.50	75.60	77.40	83.60	80.96
CARL [43]	78.10	88.00	82.90	70.20	83.40	77.30	72.90	85.70	75.40	85.00	90.80	83.00	77.80	91.70	81.59
CheXNet [44]	77.95	88.16	82.68	68.94	83.07	78.14	73.54	85.13	75.42	84.96	92.49	82.19	79.25	93.23	81.80
DualCheXNet [45]	78.40	88.80	83.10	70.50	83.80	79.60	72.70	87.60	74.60	85.20	94.20	83.70	79.60	91.20	82.36
LLAGNet [5]	78.30	88.50	83.40	70.30	84.10	79.00	72.90	87.70	75.40	85.10	93.90	83.20	79.80	91.60	82.37
Wang et al. [46]	77.90	89.50	83.60	71.00	83.40	77.70	73.70	87.80	75.90	85.50	93.30	83.80	79.10	93.80	82.57
Yan et al. [47]	79.24	88.14	84.15	70.95	84.70	81.05	73.97	87.59	75.98	84.70	94.22	83.26	80.83	93.41	83.01
Luo et al. [48]	78.91	90.69	84.18	71.84	83.76	79.85	74.19	90.63	76.81	86.10	93.96	83.81	80.36	93.71	83.49
Arias-Garzon et al. [49]	80.43	88.93	86.89	70.10	83.63	78.92	75.07	85.59	80.17	87.71	85.72	81.68	77.67	82.48	81.79
Ouyang et al. [6]	77.00	87.00	83.00	71.00	83.00	79.00	72.00	88.00	74.00	84.00	94.00	83.00	79.00	91.00	81.79
SDFN [50]	78.10	88.50	83.20	70.00	81.50	76.50	71.90	86.60	74.30	84.20	92.10	83.50	79.10	91.10	81.47
Keidar et al. [51]	80.64	90.88	86.94	70.60	83.93	77.07	76.53	85.54	80.43	89.20	90.87	81.47	78.02	91.80	83.14
MANet [52]	81.43	89.35	86.30	70.04	83.36	77.76	75.29	85.46	80.23	88.56	85.23	82.82	76.82	92.10	82.84
Proposed model	82.38	91.36	88.46	70.99	85.12	79.16	78.54	87.35	80.86	89.72	92.04	83.55	78.42	91.83	84.27

Here, Atel = Atelectasis, Card = Cardiomegaly, Effu = Effusion, Infi = Infiltration, Nodu = Nodule, Pne1 = Pneumonia, Pne2 = Pneumothorax, Cons = Consolidation, Edem = Edema, Emph = Emphysema, Fibr = Fibrosis, PT = Pleural Thickening, Hern = Hernia

TABLE III

COMPARISON OF DISEASE CLASSIFICATION AUC SCORES (%) OF THE PROPOSED MODEL AND SOTA MODELS ON THE CHEXPERT DATASET. THE BEST RESULTS ARE SHOWN IN BOLD FONT.

Model	Atelectasis	Cardiomegaly	Effusion	Consolidation	Edema	Mean
EfficientNet B0 [53]	81.78	84.01	93.09	94.15	92.79	89.16
Resnet18 [54]	84.70	87.53	91.77	93.05	92.63	89.94
DenseNet121 [32]	83.19	87.56	93.65	94.08	93.33	90.36
Proposed model	86.21	88.11	92.36	92.26	94.15	90.62

V. EXPERIMENTAL RESULTS

A. Disease Classification

1) *Ablation Study*: Table I shows the ablation study on the NIH ChestX-ray14 dataset of our trained model for different thoracic abnormalities. The baseline DenseNet121 model shows a mean AUC score of 84.12, which performed better for classifying diseases like Nodule, Edema, and Fibrosis. To provide attention to the feature maps, we downsampled our mask to the dimension of the feature map. Since nodule, edema,

and fibrosis occurs in small areas of the CXR image, the performance of our model is slightly reduced for these diseases compared to the baseline model. When we used APAM with the probabilistic disease-specific mask, we obtained improved classification results for atelectasis, consolidation, and pleural thickening. Again, when we included both chest ROI mask attention and anomaly probabilistic mask with APAM, our AUC scores improved for diseases like pneumonia, emphysema, and hernia. The mean AUC score is also higher than other models for the inclusion of the chest ROI mask and probability map

with APAM, which is 84.27.

2) Performance Comparison with SOTA Methods: Table II compares the AUC score of our best-performing model (APAM with probabilistic masks) with other state-of-the-art (SOTA) models on NIH ChestX-ray14 dataset. Here, we observe that the proposed model's performance is superior to existing SOTA methods in terms of the mean AUC score. More specifically, it has shown performance improvement in diseases like Atelectasis, Cardiomegaly, Effusion, Mass, Pneumonia, Consolidation, and Edema.

Table III shows the comparison of our proposed model (APAM with anomaly probabilistic masks and chest ROI mask) with existing models, including Resnet18 [54], EfficientNet B0 [53] and DenseNet121 [32] on CheXpert dataset where the results were obtained using the same experimental environment as used for our model. Here, we have used the same probabilistic masks which were generated for training on NIH CheXpert dataset. The results show that the proposed method provides superior results for the diseases of atelectasis and cardiomegaly, whereas performance was slightly degraded for effusion. However, the overall mean AUC score has improved compared to the other models. Our method shows a score of 90.62%, whereas the DenseNet121 yields 90.36%.

B. Abnormality Localization

1) Ablation Study: Table IV and V show the results of our ablation study in terms of localization performance using two different thresholds. The baseline model of DenseNet-121 shows a mean accuracy of 55.54% and 52.59% with IOU thresholds of 0.1 and 0.3, respectively. Here, we can see a notable performance improvement after including the proposed APAM using only the disease probabilistic mask with APAM. Our model yields accuracy scores of 64.43% and 61.73% with IOU thresholds of 0.1 and 0.3, respectively. Additionally, we can observe that using FPN (concatenation) along with APAM shows greater performance improvement in the localization tasks for diseases with small spatial features (e.g., mass, nodule, pneumothorax). Since FPN enhances the spatial resolution of the feature map, we expect that diseases like mass, nodule, and pneumothorax that occupy a small region in the image were detected easily by the model.

2) Performance Comparison with SOTA Methods: Table VI shows a comparison of the localization score of our best-performing model (APAM with probabilistic masks) and some SOTA models. Here, we observe that the proposed model shows significantly improved results compared to SOTA models for the IoU threshold of 0.3. Furthermore, our model achieves overall performance improvement, especially for nodule, pneumonia, and pneumothorax for both IoU thresholds. Activation maps generated on NIH ChestX-ray8 dataset is shown in Fig. 6.

C. Discussions

We make several observations by analyzing the extensive experimental evaluation results described in the previous sections. Firstly, incorporating the proposed APAM within an existing CNN can simultaneously improve the classification

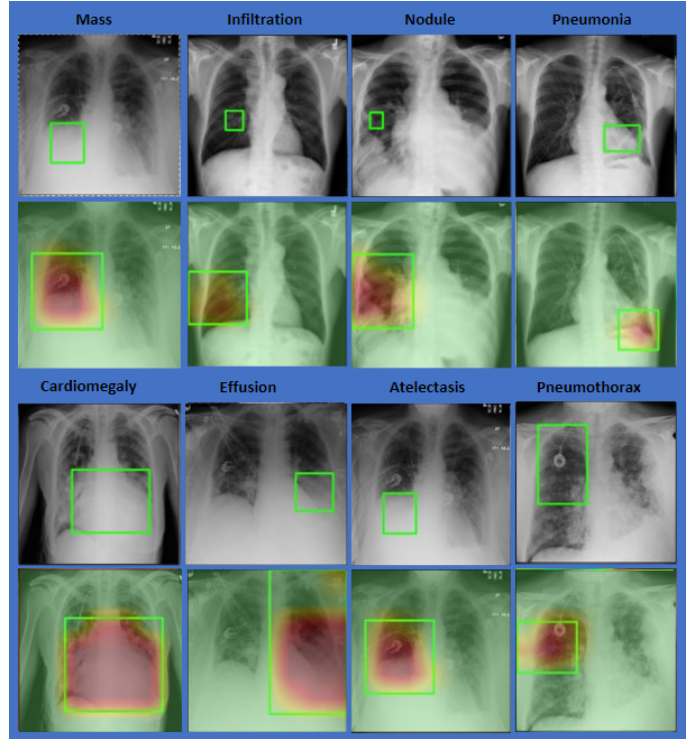


Fig. 6. Examples of some disease localization by our proposed method. First and third panel: Examples of input CXR images with ground truth bounding-box label, Second and fourth panel: Corresponding activation maps and bounding boxes of the example CXR images generated with the proposed method.

and localization performance of the CNN. Either an anatomical segmentation mask or the disease-specific probabilistic mask or both can be used for this approach. We also observe that using FPN to enhance the spatial resolution of feature maps before providing attention using APAM can improve the localization score of diseases with small spatial features.

Overall, the experimental results demonstrate the superiority of the proposed method compared to existing methods, both in terms of disease classification and localization performance. The proposed method is generic, as the APAM can be incorporated into other models to classify and localize region-specific diseases, particularly when disease localization annotations are provided with the dataset.

VI. CONCLUSION

In this work, we present a novel attention module based on disease-specific anatomy prior probability maps and chest ROI masks to simultaneously address the CXR image classification and abnormality localization problem. We evaluate our method on two publicly available datasets, NIH ChestX-ray14 and Stanford CheXpert and compare the results with recent state-of-the-art methods. Extensive experiments show that incorporating the proposed APAM with a traditional CNN backbone enhances the model's performance on both classification and localization tasks.

REFERENCES

[1] J. B. Soriano, P. J. Kendrick, K. R. Paulson, V. Gupta, E. M. Abrams, R. A. Adedoyin, T. B. Adhikari, S. M. Advani, A. Agrawal, E. Ahmadian

TABLE IV

ABLATION STUDY WITH RESPECT TO DISEASE LOCALIZATION PERFORMANCE USING $T(\text{IOU}) = 0.1$ FOR THE PROPOSED MODELS ON THE NIH DATASET. THE BEST RESULTS ARE SHOWN IN BOLD FONT.

Model				Localization Score (%)								
FPN_T	FPN_C	AM (AbM)	AM (LM)	Atel	Card	Effu	Infi	Mass	Nodu	Pne1	Pne2	Mean
Baseline				42.50	73.30	25.11	36.02	67.27	64.66	78.75	56.70	55.54
✓				52.61	78.98	19.66	42.27	68.64	68.07	86.36	55.23	58.98
	✓			52.61	85.00	15.45	31.70	72.16	71.14	86.14	65.34	59.94
		✓		54.20	85.45	37.84	52.05	67.50	67.39	84.66	66.36	64.43
			✓	34.66	73.18	9.66	28.07	55.68	66.70	76.59	50.23	49.35
✓		✓		52.27	88.86	10.45	28.18	74.66	76.25	86.36	71.02	61.01
	✓	✓		55.11	87.50	19.32	32.39	75.68	78.30	86.36	73.86	63.57
		✓	✓	48.52	77.73	20.23	43.52	64.55	68.75	79.20	59.77	57.78
✓				6.36	55.80	5.91	6.59	26.02	16.48	40.45	32.50	23.76
	✓			5.80	53.52	5.34	4.43	14.20	7.39	30.45	27.73	18.61
✓		✓	✓	49.77	87.05	9.20	44.89	65.34	75.45	86.36	61.82	59.99
	✓	✓	✓	54.89	73.07	7.84	37.73	61.93	76.14	86.36	62.95	57.61

Here, FPN_T = Traditional FPN, FPN_C = FPN Using Concatenation, AM (AbM) = APAM Utilizing Probabilistic Abnormality Mask, AM(LM) = APAM Utilizing Chest ROI Mask, Atel = Atelectasis, Card = Cardiomegaly, Effu = Effusion, Infi = Infiltration, Nodu = Nodule, Pne1 = Pneumonia, Pne2 = Pneumothorax

TABLE V

ABLATION STUDY WITH RESPECT TO DISEASE LOCALIZATION PERFORMANCE USING $T(\text{IOU}) = 0.3$ FOR THE PROPOSED MODELS ON THE NIH DATASET. THE BEST RESULTS ARE SHOWN IN BOLD FONT.

Model				Localization Score (%)								
FPN_T	FPN_C	AM (AbM)	AM (LM)	Atel	Card	Effu	Infi	Mass	Nodu	Pne1	Pne2	Mean
Baseline				39.09	72.27	19.66	30.91	64.89	64.55	75.68	53.64	52.59
✓				49.77	75.34	14.43	37.50	67.27	67.95	86.36	52.39	56.38
	✓			50.11	80.91	10.80	27.61	70.45	71.02	85.80	62.61	57.41
		✓		50.68	84.66	32.16	46.93	65.34	67.27	83.41	63.41	61.73
✓				31.70	72.16	4.66	22.61	53.98	66.70	75.00	47.27	46.76
	✓	✓		50.11	85.68	6.25	25.11	73.64	76.25	86.36	67.84	58.91
		✓	✓	53.07	83.98	14.89	28.41	74.32	78.30	86.36	70.57	61.24
✓				44.32	76.82	14.20	36.82	62.50	68.75	77.84	56.48	54.72
	✓			5.45	44.09	1.70	53.75	25.34	16.48	40.45	31.02	21.04
✓				54.89	41.70	51.36	52.16	13.30	57.39	30.23	25.91	15.87
✓		✓	✓	46.93	83.64	54.89	40.11	63.86	75.45	86.36	58.75	57.50
	✓	✓	✓	52.16	67.73	52.84	33.18	60.80	76.14	86.36	59.77	54.87

Here, FPN_T = Traditional FPN, FPN_C = FPN Using Concatenation, AM (AbM) = APAM Utilizing Probabilistic Abnormality Mask, AM(LM) = APAM Utilizing Chest ROI Mask, Atel = Atelectasis, Card = Cardiomegaly, Effu = Effusion, Infi = Infiltration, Nodu = Nodule, Pne1 = Pneumonia, Pne2 = Pneumothorax

TABLE VI

COMPARISON OF DISEASE LOCALIZATION ACCURACY (%) OF THE BEST PERFORMING PROPOSED MODEL WITH STATE-OF-THE-ART METHODS. THE BEST RESULTS ARE SHOWN IN BOLD FONT.

T(IoU)	Model	Atelectasis	Cardiomegaly	Effusion	Infiltration	Mass	Nodule	Pneumonia	Pneumothorax	Mean
0.1	Li et. al. [39]	59.0	81.0	73.0	85.0	69.0	29.0	23.0	38.0	57.0
	Liu et. al. [55]	39.0	90.0	65.0	85.0	69.0	38.0	30.0	39.0	60.0
	Ouyang et. al. [26]	78.0	97.0	82.0	85.0	78.0	56.0	76.0	48.0	75.0
	Proposed model	54.0	85.0	37.0	52.0	67.0	67.0	84.0	66.0	64.0
0.3	Liu et. al. [55]	34.0	71.0	39.0	65.0	48.0	9.0	16.0	20.0	38.0
	Ouyang et. al. [26]	34.0	40.0	27.0	55.0	51.0	14.0	42.0	22.0	36.0
	Proposed model	50.0	84.0	32.0	46.0	65.0	67.0	83.0	63.0	61.0

et al., "Prevalence and attributable health burden of chronic respiratory diseases, 1990–2017: a systematic analysis for the global burden of disease study 2017," *Lancet Respir. Med.*, vol. 8, no. 6, pp. 585–596, 2020.

[2] "Rise in global deaths and disability due to lung diseases over past three decades" [Online]. Available: <https://www.bmjjournals.org/company/newsroom/rise-in-global-deaths-and-disability-due-to-lung-diseases-over-past-three-decades/>

[3] B. S. Kelly, L. A. Rainford, S. P. Darcy, E. C. Kavanagh, and R. J. Toohey, "The development of expertise in radiology: in chest radiograph interpretation, 'expert' search pattern may predate 'expert' levels of diagnostic accuracy for pneumothorax identification," *Radiology*, vol. 280, no. 1, pp. 252–260, 2016.

[4] J. Cai, L. Lu, A. P. Harrison, X. Shi, P. Chen, and L. Yang, "Iterative attention mining for weakly supervised thoracic disease pattern local-

ization in chest x-rays," in *MICCAI*. Springer, 2018, pp. 589–598.

[5] B. Chen, J. Li, G. Lu, and D. Zhang, "Lesion location attention guided network for multi-label thoracic disease classification in chest x-rays," *IEEE J. Biomed. Health Inform.*, vol. 24, no. 7, pp. 2016–2027, 2019.

[6] X. Ouyang, S. Karanam, Z. Wu, T. Chen, J. Huo, X. S. Zhou, Q. Wang, and J.-Z. Cheng, "Learning hierarchical attention for weakly-supervised chest x-ray abnormality localization and diagnosis," *IEEE Trans. Med. Imaging*, vol. 40, no. 10, pp. 2698–2710, 2020.

[7] B. Chen, Z. Zhang, J. Lin, Y. Chen, and G. Lu, "Two-stream collaborative network for multi-label chest x-ray image classification with lung segmentation," *Pattern Recognit. Lett.*, vol. 135, pp. 221–227, 2020.

[8] U. Kamal, M. Zunaed, N. B. Nizam, and T. Hasan, "Anatomy-xnet: An anatomy aware convolutional neural network for thoracic disease classification in chest x-rays," *IEEE J. Biomed. Health. Inform.*, vol. 26, no. 11, 2022.

[9] J. Hu, L. Shen, S. Albanie, G. Sun, and E. Wu, "Squeeze-and-Excitation Networks," *IEEE Trans. Pattern Anal.*, vol. 42, no. 8, pp. 2011–2023, 8 2020.

[10] J. Hu, L. Shen, S. Albanie, G. Sun, and A. Vedaldi, "Gather-excite: Exploiting feature context in convolutional neural networks," *Adv. Neural Inf. Process Syst.*, vol. 31, 2018.

[11] B. Chen, Y. Huang, Q. Xia, and Q. Zhang, "Nonlocal spatial attention module for image classification," *Int. J. Adv. Robot.*, vol. 17, no. 5, p. 1729881420938927, 2020.

[12] B. Zhou, A. Khosla, A. Lapedriza, A. Oliva, and A. Torralba, "Learning deep features for discriminative localization," in *Proc. IEEE Int. Conf. Comput. Vis.*, 2016, pp. 2921–2929.

[13] R. R. Selvaraju, M. Cogswell, A. Das, R. Vedantam, D. Parikh, and D. Batra, "Grad-cam: Visual explanations from deep networks via gradient-based localization," in *Proc. IEEE Int. Conf. Comput. Vis.*, 2017, pp. 618–626.

[14] A. Chattopadhyay, A. Sarkar, P. Howlader, and V. N. Balasubramanian, "Grad-cam++: Generalized gradient-based visual explanations for deep convolutional networks," in *IEEE Winter Conf. Appl. Comput. Vis.* IEEE, 2018, pp. 839–847.

[15] H. Wang, Z. Wang, M. Du, F. Yang, Z. Zhang, S. Ding, P. Mardziel, and X. Hu, "Score-CAM: Score-Weighted Visual Explanations for Convolutional Neural Networks," in *Proc. CVPR*. IEEE, 6 2020, pp. 111–119.

[16] H. Wang, R. Naidu, J. Michael, and S. S. Kundu, "Ss-cam: Smoothed score-cam for sharper visual feature localization," *arXiv preprint arXiv:2006.14255*, 2020.

[17] R. Fu, Q. Hu, X. Dong, Y. Guo, Y. Gao, and B. Li, "Axiom-based grad-cam: Towards accurate visualization and explanation of cnns," *arXiv preprint arXiv:2008.02312*, 2020.

[18] W. Ye, J. Yao, H. Xue, and Y. Li, "Weakly supervised lesion localization with probabilistic-cam pooling," *arXiv preprint arXiv:2005.14480*, 2020.

[19] S. Xu, D. Chang, J. Xie, and Z. Ma, "GRAD-CAM Guided Channel-Spatial Attention Module for Fine-Grained Visual Classification," in *2021 IEEE 31st Int. WORKS Mach.* IEEE, 10 2021, pp. 1–6.

[20] G. S. Lodwick, "Computer-aided diagnosis in radiology: A research plan," *Invest. Radiol.*, vol. 1, no. 1, pp. 72–80, 1966.

[21] X. Wang, Y. Peng, L. Lu, Z. Lu, M. Bagheri, and R. M. Summers, "Chestx-ray8: Hospital-scale chest x-ray database and benchmarks on weakly-supervised classification and localization of common thorax diseases," in *Proc. IEEE Int. Conf. Comput. Vis.*, 2017, pp. 2097–2106.

[22] S. Guendel, S. Grbic, B. Georgescu, S. Liu, A. Maier, and D. Comaniciu, "Learning to recognize abnormalities in chest x-rays with location-aware dense networks," in *Iberoam. Congr. Pattern Recognit.* Springer, 2018, pp. 757–765.

[23] I. M. Baltruschat, H. Nickisch, M. Grass, T. Knopp, and A. Saalbach, "Comparison of deep learning approaches for multi-label chest x-ray classification," *Sci. Rep.*, vol. 9, no. 1, pp. 1–10, 2019.

[24] Y. Tang, X. Wang, A. P. Harrison, L. Lu, J. Xiao, and R. M. Summers, "Attention-guided curriculum learning for weakly supervised classification and localization of thoracic diseases on chest radiographs," in *Int. WORKS Mach. Learn. Med. Imaging*. Springer, 2018, pp. 249–258.

[25] L. Yao, J. Prosky, E. Poblenz, B. Covington, and K. Lyman, "Weakly supervised medical diagnosis and localization from multiple resolutions," *arXiv preprint arXiv:1803.07703*, 2018.

[26] X. Ouyang, S. Karanam, Z. Wu, T. Chen, J. Huo, X. S. Zhou, Q. Wang, and J.-Z. Cheng, "Learning hierarchical attention for weakly-supervised chest x-ray abnormality localization and diagnosis," *IEEE Trans. Med. Imaging*, vol. 40, no. 10, pp. 2698–2710, 2020.

[27] O. Ronneberger, P. Fischer, and T. Brox, "U-net: Convolutional networks for biomedical image segmentation," in *MICCAI*. Springer, 2015, pp. 234–241.

[28] J. Shiraishi, S. Katsuragawa, J. Ikezoe, T. Matsumoto, T. Kobayashi, K.-i. Komatsu, M. Matsui, H. Fujita, Y. Kodera, and K. Doi, "Development of a digital image database for chest radiographs with and without a lung nodule: receiver operating characteristic analysis of radiologists' detection of pulmonary nodules," *AJR Am. J. Roentgenol.*, vol. 174, no. 1, pp. 71–74, 2000.

[29] F. P. Preparata and S. J. Hong, "Convex hulls of finite sets of points in two and three dimensions," *Communications of the ACM*, vol. 20, no. 2, pp. 87–93, 1977.

[30] S. Woo, J. Park, J.-Y. Lee, and I. S. Kweon, "Cbam: Convolutional block attention module," in *Proc. of ECCV*, 2018, pp. 3–19.

[31] A. L. Maas, A. Y. Hannun, and A. Y. Ng, "Rectifier nonlinearities improve neural network acoustic models," in *ICML WORKS WDLASL*, 2013.

[32] G. Huang, Z. Liu, L. Van Der Maaten, and K. Q. Weinberger, "Densely connected convolutional networks," in *Proc. IEEE Int. Conf. Comput. Vis.*, 2017, pp. 4700–4708.

[33] T.-Y. Lin, P. Dollár, R. Girshick, K. He, B. Hariharan, and S. Belongie, "Feature pyramid networks for object detection," in *Proc. IEEE Int. Conf. Comput. Vis.*, 2017, pp. 2117–2125.

[34] J. Redmon and A. Farhadi, "Yolov3: An incremental improvement," *arXiv preprint arXiv:1804.02767*, 2018.

[35] J. Irvin, P. Rajpurkar, M. Ko, Y. Yu, S. Ciurea-Ilcus, C. Chute, H. Marklund, B. Haghgoo, R. Ball, K. Shpanskaya *et al.*, "Chexpert: A large chest radiograph dataset with uncertainty labels and expert comparison," in *Proc. Innov. Appl. Artif.*, vol. 33, no. 01, 2019, pp. 590–597.

[36] J. Deng, W. Dong, R. Socher, L.-J. Li, Kai Li, and Li Fei-Fei, "ImageNet: A large-scale hierarchical image database," in *Proc. CVPR*. IEEE, 6 2009, pp. 248–255.

[37] D. P. Kingma and J. Ba, "Adam: A method for stochastic optimization," *arXiv preprint arXiv:1412.6980*, 2014.

[38] S. Suzuki and K. be, "Topological structural analysis of digitized binary images by border following," *Comput. graph.*, vol. 30, no. 1, pp. 32–46, 4 1985.

[39] Z. Li, C. Wang, M. Han, Y. Xue, W. Wei, L.-J. Li, and L. Fei-Fei, "Thoracic disease identification and localization with limited supervision," in *Proc. IEEE Int. Conf. Comput. Vis.*, 2018, pp. 8290–8299.

[40] L. Yao, E. Poblenz, D. Dagunts, B. Covington, D. Bernard, and K. Lyman, "Learning to diagnose from scratch by exploiting dependencies among labels," *arXiv preprint arXiv:1710.10501*, 2017.

[41] X. Wang, Y. Peng, L. Lu, Z. Lu, and R. M. Summers, "Tienet: Text-image embedding network for common thorax disease classification and reporting in chest x-rays," in *Proc. IEEE Int. Conf. Comput. Vis.*, 2018, pp. 9049–9058.

[42] T. K. Khanh Ho and J. Gwak, "Multiple feature integration for classification of thoracic disease in chest radiography," *Appl. Sci.*, vol. 9, no. 19, p. 4130, 2019.

[43] Q. Guan and Y. Huang, "Multi-label chest x-ray image classification via category-wise residual attention learning," *Pattern Recognit. Lett.*, vol. 130, pp. 259–266, 2020.

[44] P. Rajpurkar, J. Irvin, K. Zhu, B. Yang, H. Mehta, T. Duan, D. Ding, A. Bagul, C. Langlotz, K. Shpanskaya *et al.*, "Chexnet: Radiologist-level pneumonia detection on chest x-rays with deep learning," *arXiv preprint arXiv:1711.05225*, 2017.

[45] B. Chen, J. Li, X. Guo, and G. Lu, "Dualchexnet: dual asymmetric feature learning for thoracic disease classification in chest x-rays," *Biomed. Signal Process. Con.*, vol. 53, p. 101554, 2019.

[46] H. Wang, S. Wang, Z. Qin, Y. Zhang, R. Li, and Y. Xia, "Triple attention learning for classification of 14 thoracic diseases using chest radiography," *Med. Image Anal.*, vol. 67, p. 101846, 2021.

[47] C. Yan, J. Yao, R. Li, Z. Xu, and J. Huang, "Weakly supervised deep learning for thoracic disease classification and localization on chest x-rays," in *ACM-BCB*, 2018, pp. 103–110.

[48] L. Luo, L. Yu, H. Chen, Q. Liu, X. Wang, J. Xu, and P.-A. Heng, "Deep mining external imperfect data for chest x-ray disease screening," *IEEE Trans. Med. Imaging*, vol. 39, no. 11, pp. 3583–3594, 2020.

[49] D. Arias-Garzón, J. A. Alzate-Grisales, S. Orozco-Arias, H. B. Arteaga-Arteaga, M. A. Bravo-Ortiz, A. Mora-Rubio, J. M. Saborit-Torres, J. A. M. Serrano, M. de la Iglesia Vayá, O. Cardona-Morales *et al.*, "Covid-19 detection in x-ray images using convolutional neural networks," *MLWA*, vol. 6, p. 100138, 2021.

[50] H. Liu, L. Wang, Y. Nan, F. Jin, Q. Wang, and J. Pu, "Sdfn: Segmentation-based deep fusion network for thoracic disease classification in chest x-ray images," *Comput. Med. Imaging Graph.*, vol. 75, pp. 66–73, 2019.

[51] D. Keidar, D. Yaron, E. Goldstein, Y. Shachar, A. Blass, L. Charbinsky, I. Aharony, L. Lifshitz, D. Lumelsky, Z. Neeman *et al.*, "Covid-19 classification of x-ray images using deep neural networks," *Eur. Radiol.*, vol. 31, no. 12, pp. 9654–9663, 2021.

[52] Y. Xu, H.-K. Lam, and G. Jia, "Manet: A two-stage deep learning method for classification of covid-19 from chest x-ray images," *Neurocomputing*, vol. 443, pp. 96–105, 2021.

[53] M. Tan and Q. Le, "Efficientnet: Rethinking model scaling for convolutional neural networks," in *Proc. Int. Conf. Mach. Learn.* PMLR, 2019, pp. 6105–6114.

[54] K. He, X. Zhang, S. Ren, and J. Sun, "Deep residual learning for image recognition," in *Proc. IEEE Int. Conf. Comput. Vis.*, 2016, pp. 770–778.

[55] J. Liu, G. Zhao, Y. Fei, M. Zhang, Y. Wang, and Y. Yu, "Align, attend and locate: Chest x-ray diagnosis via contrast induced attention network with limited supervision," in *Proc. IEEE Int. Conf. Comput. Vis.*, 2019, pp. 10 632–10 641.